Journal of Materials Chemistry A

Accepted Manuscript

ROYAL SOCIETY OF CHEMISTRY

www.rsc.org/materialsA

Journal Name

ARTICLE

One-Step Synthesis of Silicon/Hematite@Carbon Hybrid Nanosheets/Silicon Sandwich-Like Composite as Anode Material for Li-ion Batteries

Received 00th January 20xx,
Accepted 00th January 20xx

DOI: 10.1039/x0xx00000x

www.rsc.org/

Lei Zhang,[a] Haipeng Guo,[a] Ranjusha Rajagopalan,[a] Xianluo Hu,[b] Yunhui Huang,[b] Shi Xue Dou[a] and Hua Kun Liu[a]*

Silicon and hematite, both important functional materials with high theoretical capacity, have been intensively investigated separately for application as anode materials in lithium ion batteries (LIBs). The main challenges associated with these anode materials are their low electronic conductivity and structural degradation caused by large volume expansion during cycling, which are not tolerable for future LIBs with high energy density and large power output. Active particles anchored in a porous conductive skeleton are widely used for improving the electrochemical performance of silicon as well as that of hematite. Herein, we develop a novel-structured carbon-silicon-hematite anode material via a single-step technique that addresses these problems. In the resultant architecture, silicon nanoparticles are sandwiched between the iron-oxide-embedded porous carbon sheets. The flexible and conductive carbon sheets improve the conductivity and accommodate the volume changes of the embedded hematite and silicon nanoparticles, and thus maintain structural and electrical integrity. Meanwhile, the void space between the carbon layers leaves enough room for the expansion and contraction of silicon during the lithiation and delithiation processes. High capacity (~1980 mAh g^{-1} at 750 mA g^{-1}) and long cycle life (250 cycles) have been achieved for this sandwich-like carbon-silicon-hematite electrode.

1. Introduction

Conventional lithium ion batteries (LIBs) based on carbon anodes, such as commercial graphite microspheres and mesophase carbon microbeads (MCMB), with theoretical capacity of about 372 mAh g^{-1}, have now reached their limit in terms of meeting the need for high energy storage.[1-4] To meet the increasing demand for energy storage capability, novel electrode materials with higher capacity, low cost, and the ability to be produced on a large scale are of great interest.[5]

Silicon (Si) and hematite (α-Fe_2O_3) have long been regarded as appealing anode materials for LIBs because of their much higher theoretical capacities (~4200 and 1007 mAh g^{-1}, respectively) than those of the commercially used ones, as well as their nontoxicity and natural abundance.[3,6-14] Despite all of these advantages, the full utilization of silicon- or α-Fe_2O_3-based batteries to date has been hindered by a series of obstacles, including poor cycle life and rate performance, that resulted from their large volumetric expansion during cycling and low ionic/electronic conductivity.[15-19] Hence, great efforts have been made to further improve their electrochemical performance by using various silicon-containing (silicon nanowires,[10,20-21] silicon nanotubes,[22] porous structured silicon,[23] and carbon coated silicon[24-25]) or α-Fe_2O_3-containing (Fe_2O_3 nanorods,[15] Fe_2O_3 nanotubes,[26] Fe_2O_3 nanosheets,[6] graphene@Fe_2O_3 composite[9]) materials. Among them, porous carbon@Si or carbon@α-Fe_2O_3 composites in which the active particles are coated or embedded in a porous conductive carbon skeleton are quite promising, because the void space allows the expansion of silicon and α-Fe_2O_3 during the lithiation/ delithiation processes, thus maintaining the structural and electrical integrity.[7] For instance, Cui et al. demonstrated a carbon@void@Si (yolk-shell) composite system having a high capacity of ~2800 mAh g^{-1}.[27] α-Fe_2O_3/reduced graphene oxide (rGO) nanocomposites (~1100 mAh g^{-1}) in which the α-Fe_2O_3 nanoparticles were uniformly anchored on the graphene nanosheets were fabricated by Zhang et al.[28] through a facile microwave hydrothermal method. Therefore, the main problem for silicon and α-Fe_2O_3 can be addressed by combining porosity and the incorporation of carbon in one structure. Till now, some work has been reported that combining silicon with metal oxide or alloys in one system is an effective way to improve the electrochemical performance of the synthesized electrodes by taking advantages of the superiorities of both silicon and the active additions, such as Co_2O_3@Si,[29] SnO_2@Si,[30] Fe_3C@Si,[31] and

[a] Institute for Superconducting and Electronic Materials, University of Wollongong, Wollongong, NSW 2522, Australia.
[b] State Key Laboratory of Materials Processing and Die & Mould Technology, School of Materials Science and Engineering, Huazhong University of Science and Technology, Wuhan 430074, P. R. China.
† Distinguished Professor Huakun Liu, Corresponding Author.
Electronic Supplementary Information (ESI) available: See DOI: 10.1039/x0xx00000x

Ge@Si.[32] It is found that, the specific capacities of the composites were increased due to the introduction of silicon, and the cycling stability was also improved from the specific structure of the metal oxide or alloys. However, to the best of our knowledge, most of the composite anodes explored so far containing either silicon or α-Fe_2O_3 along with carbon, and only few reports are available in which both the materials are utilized in one system. Just as reported this year, David Zitoun synthesized Si@hollow γ-Fe2O3 nanoparticles as anode for LIBs.[33] As reported, the prepared Si with iron oxide grown on its surface showed a very high specific capacity (around 2600 mAh g^{-1}).However, the preparation process of this work is very complex and high cost. In addition, without the introduction of carbon or other kinds of conductive additions, the conductivity of this prepared composite is low. Therefore, it is envisioned that advances in LIBs technology can be achieved by incorporating both silicon and α-Fe_2O_3 in one porous carbon skeleton.

Herein, we report a facile one-step synthesis of a carbon-silicon-hematite (C-Si-Fe_2O_3) composite. In our case, silicon nanoparticles (Si NPs) are sandwiched between α-Fe_2O_3-embedded porous carbon sheets (C@Fe_2O_3). The electronic conductivity of both the silicon and the α-Fe_2O_3 NPs can be improved by the conductive carbon layers.[34,35] Meanwhile, the flexible carbon sheets are adaptable and can freely switch between the expansion and contraction of the active particles upon lithiation and delithiation.[28,36] In addition, the space between the carbon layers allows the Si NPs to expand freely,[37] and the C@Fe_2O_3 layers can prevent the Si and α-Fe_2O_3 nanoparticles from aggregating. These unique characteristics facilitate the collection and transport of electrons, resulting in high capacity and good cycling stability.[38,39]

2. Experiment section

2.1. Material synthesis

In this work, 0.36 g iron (III) chloride hexahydrate ($FeCl_3·6H_2O$, 1.33 mmol, Sigma-Aldrich, 98%) was dissolved in 1.22 g oleic acid, which was treated as the carbon precursor (Sigma-Aldrich). The resulting mixture was aged at 85 °C for 3 h to obtain the bronzing slurry, and then mixed with 600 mg Si (～100 nm). The mixture was heated to 600 °C at the heating rate of 5 °C min^{-1} under Ar atmosphere for 3 h and then washed with distilled water to obtain the final material (C-Si-Fe_2O_3). For comparison, carbon coated silicon (C-Si) composite was fabricated, in which 600 mg Si was mixed with 1.22 g oleic acid. Then, the mixture was heated to 600 °C at the heating rate of 5 °C min^{-1} under Ar atmosphere for 3 h to obtain C-Si. In addition, only $FeCl_3·6H_2O$ and oleic acid were mixed and heated under 600 °C at the heating rate of 5 °C min^{-1} under Ar atmosphere for 3 h to obtain carbon/iron oxide composite (C@Fe_2O_3).

2.2. Characterization

The products, C-Si-Fe_2O_3 and C-Si were analyzed by X-ray diffraction (XRD; GBC MMA) with Cu Kα radiation; Raman spectroscopy (JobinYvon HR800) employing a 10 mW helium/neon laser at 632.8 nm; field emission scanning electron microscopy (FESEM; JEOL 7500); and transmission electron microscopy (TEM; JEOL ARM-200F) with high-resolution TEM (HRTEM). Elemental carbon-hydrogen-nitrogen mode (CHN) analysis was conducted to determine the carbon content in C-Si-Fe_2O_3. X-ray photoelectron spectroscopy (XPS) was carried out using Al Kα radiation and the fixed analyzer transmission mode. The pass energy was 60 eV for the survey spectra and 20 eV for specific elements.

2.3. Electrochemical measurements

The tests were conducted by assembling coin-type half cells in an argon-filled glove box. Lithium foil was employed as both reference and counter electrode. The working electrode consisted of 70 wt.% active material (C-Si-Fe_2O_3 and C-Si, respectively), 20 wt.% carbon black, and 10 wt.% carboxymethyl cellulose (CMC) binder. The electrolyte was 1.0 M $LiPF_6$ in a 1:1 (v/v) mixture of ethylene carbonate (EC) and diethyl carbonate (DEC). Electrochemical cycling of coin cells was conducted at 750 mA g^{-1} using galvanostatic mode in the potential window of 10 mV to 2.8 V (vs. Li/Li^+). Cyclic voltammetry was performed using a Biologic VMP-3 electrochemical workstation between 0.01 and 2.8 V at a scan rate of 0.1 mV s^{-1}.

3. Results and discussion

Fig. S1 in the Supporting Information shows a typical scanning electron microscope (SEM) image of Si NPs, which are in the size range of around 100 nm. The obtained C-Si composite in Fig. 1(a) exhibits an interconnected network, forming a continuous three-dimensional (3D) structure. The higher magnification image of C-Si [Fig. 1(b)] shows that the Si NPs are well connected with each other through the carbon coating layers. Compared with C-Si, C-Si-Fe_2O_3 [Fig. 1(c)] shows a significantly different structure. It can be seen that C-Si-Fe_2O_3 possesses a layer-by-layer assembled structure. Si NPs are dispersed between the Fe_2O_3-embedded carbon (C@Fe_2O_3) layers, and these C@Fe_2O_3 layers prevent the aggregation of Si NPs and α-Fe_2O_3 nanoparticles during the annealing process. More importantly, some of the carbon sheets reconstitute in stacks to form a porous conductive network, and this unique interconnected 3D nanostructure not only improves the electronic conductivity, but also provides void space to accommodate the volume changes of Si NPs and α-Fe_2O_3 during cycling while maintaining the mechanical stability.[37] Fig. 1(d) shows an enlarged image of a C@Fe_2O_3 layer, where uniformly embedded α-Fe_2O_3 NPs in the size range of 30-40 nm are clearly seen on the carbon layers. Furtherly, for comparison with C-Si and C-Si-Fe_2O_3, in order to confirm the function of iron-precursor in this process, the C@Fe_2O_3 was also

prepared. According to the SEM pictures in Fig. S2, it can be found that the highly agglomerated sheet-like C@Fe_2O_3 composite was successfully obtained, which means the iron-precursor played an very important role in the formation of 2D sheet structured C@Fe_2O_3.

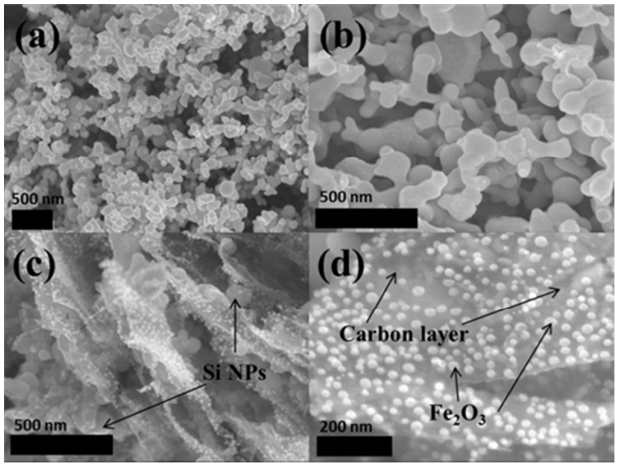

Fig. 1. SEM images of C-Si (a, b), and C-Si-Fe_2O_3 (c, d)

The energy dispersive X-ray spectroscopy (EDX) spectrum in Fig. S3(a) shows that only carbon and silicon can be found in this sample (Cu peaks arise from the specimen holder). Fig. S3(b) shows a TEM image of C-Si. It can be seen that C-Si is composed of carbon-coated Si NPs in the size range of 80-130 nm, and all of these particles are interconnected together. The enlarged TEM image of C-Si [Fig. S3(c)] shows that the silicon surface was coated by the carbon layers, which can be further tested by the elemental mapping images in [Fig. S3(d)] and [Fig. S3(e)]. It can be seen that every single silicon nanoparticle is separated from the others due to the outer carbon shell. According to the HRTEM picture in Fig. S3(f), the thickness of the carbon coating layer was around 5-8 nm. Fig. 2(a) shows that carbon, silicon, and iron can be found in C-Si-Fe_2O_3. The element mapping images [Fig. 2(c-e)] from Fig. 2(b) show that even after ultrasonication for TEM characterization, α-Fe_2O_3 particles are still firmly attached to the carbon sheets and Si NPs are also dispersed uniformly between the C@Fe_2O_3 layers. According to the enlarged TEM and the inserted HRTEM images of the individual Fe_2O_3 nanoparticle, it can be found that the size of Fe_2O_3 nanoparticles is in a range of 15-25 nm. This unique structure helps to protect the α-Fe_2O_3 and Si NPs from agglomeration and enables the good dispersion of these active particles over the carbon sheet supports. In addition, very thin carbon coating layers can be seen on the surfaces of the Si NPs.

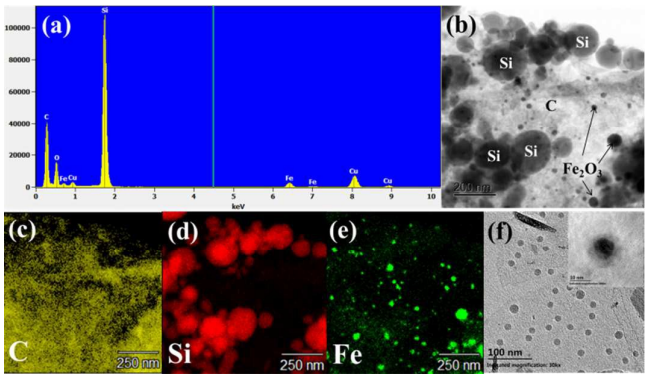

Fig. 2. C-Si-Fe_2O_3: EDX spectrum (a), TEM image with low magnification (b), corresponding carbon (yellow), silicon (red), iron (green) elemental mapping images (c, d and e), and TEM image with high magnification (f) (insert is the HRTEM of the individual Fe_2O_3 nanoparticle).

So, based on the SEM and TEM data provided above, we give the model of this prepared C-Si-Fe_2O_3 composite as shown in Fig. 3. The mechanism for the formation of this structure can be explained as follows. The iron–oleate complex was first synthesized during the aging period and then uniformly mixed with the Si NPs. Upon heating under inert atmosphere, the metal–oleate complex was converted to form the two-dimensional hematite/carbon hybrid nanosheet structure, and the thin carbon coated Si NPs were sandwiched between these hybrid nanosheets.[39,40]

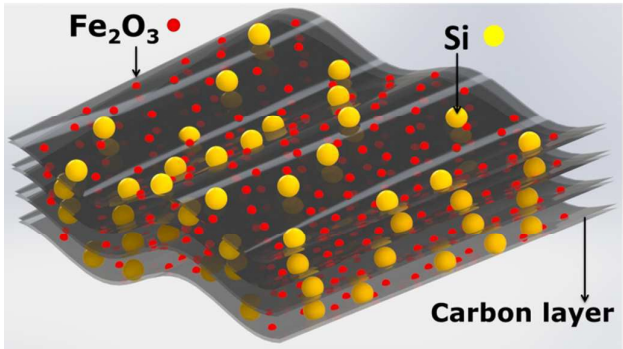

Fig. 3. Schematic of the prepared C-Si-Fe_2O_3 composite

Fig. 4(a) shows the XRD patterns of C-Si-Fe_2O_3, C-Si, and Si NPs. For all the samples, there are three distinct diffraction peaks at 2θ values of 28.3, 47.0, and 55.8°, which can be assigned to the (111), (220), and (311) planes of silicon phase (JCPDS NO. 27-1402), respectively.[16] Besides the silicon phase, in the C-Si-Fe_2O_3 sample, all the peaks at about 24.1, 33.1, 35.6, 43.3, 49.5, 54.1, 57.5, 62.3, and 65.3° can be assigned to the (012), (104), (110), (202), (024), (116), (018), (214), and (300) lattice planes, respectively, of α-Fe_2O_3 (JCPDS No. 33–0664).[28]

Fig. 4(b) presents their Raman spectra. For all the silicon-based samples, the strong peaks at about 500 cm^{-1} are ascribed to Si and SiO.[41,42] The peak at around 1350 cm^{-1} (D-band) is associated with the vibration of carbon atoms with dangling bonds in plane terminations of the activated carbon (AC),[43] while the strong peak at about 1590.0 cm^{-1} (G-band) can be assigned to the vibration of

sp^2-bonded carbon atoms in a two-dimensional hexagonal lattice,[44] namely, the stretching modes of C=C bonds in typical graphite. For the carbon-based samples, a low-intensity and weak G-band peak suggests structural imperfection of the graphene sheets, such as small crystal domain size or defects.[45-47] Therefore, the carbon inside C-Si-Fe_2O_3 and C-Si belongs to the AC class and has a low degree of graphitization. Compared with Si NPs, it can be seen that the peaks around 292 and 606 cm^{-1} of C-Si-Fe_2O_3 have stronger intensity. This increased intensity is due to the overlap of peaks of α-Fe_2O_3 and silicon at these positions, indicating the presence of α-Fe_2O_3. In agreement with the XRD results, this indicates that the C-Si-Fe_2O_3 composite was successfully synthesized via our facile one-step method.

The components of C-Si-Fe_2O_3 were further confirmed by X-ray photoelectron spectroscopy (XPS), suggesting the presence of the elements Si, C, O, and Fe in the sample [see Fig. 4(c)]. A high resolution spectrum of Fe 2p is displayed in Figure 4(d), showing two peaks at about 712.0 and 725.0 eV, corresponding to Fe $2p_{3/2}$ and Fe $2p_{1/2}$.[48] The carbon content of C-Si-Fe_2O_3 was measured using a carbon-hydrogen-nitrogen (CHN) analyzer. 15 wt.% carbon was found in C-Si-Fe_2O_3. Based on the ratio of $FeCl_3 \cdot 6H_2O$ to the Si NPs, the α-Fe_2O_3 and silicon content of C-Si-Fe_2O_3 was calculated to be around 20 and 65 wt.%, respectively.

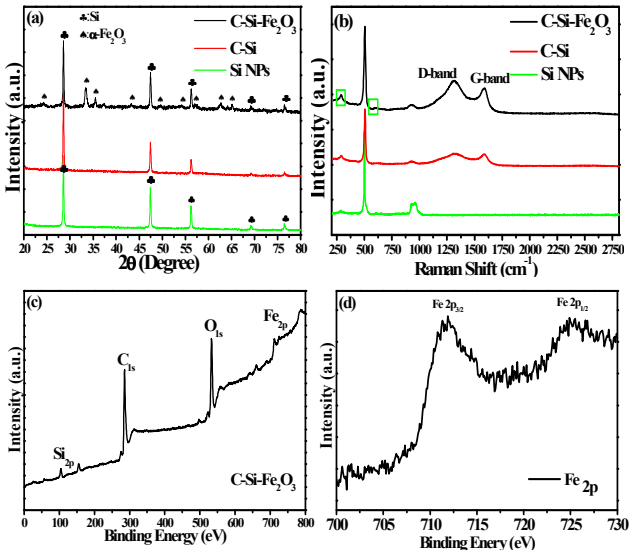

Fig. 4. XRD patterns (a) and Raman spectra (b) of all the samples; XPS survey spectrum of C-Si-Fe_2O_3 (c) and the corresponding high resolution XPS spectrum of Fe 2p (d)

Fig. 5(a) shows the charge/discharge curves of C-Si-Fe_2O_3 and C-Si at a current density of 750 mA g^{-1}. The discharge and charge capacities in the first run are about 2846.5 and 1911.4 mAh g^{-1} for C-Si-Fe_2O_3, and 3404.3 and 2206.9 mAh g^{-1} for C-Si, so that their initial coulombic efficiency is 67.2 and 64.8 %, respectively. The low initial coulombic efficiency of the synthesized C-Si-Fe_2O_3 may be because of the porous structure and secondary reactions such as electrolyte decomposition between the electrode and electrolyte, which often result in high irreversibility.[49-51]

Fig. 5(b) shows the representative first three consecutive cyclic voltammetry (CV) curves of C-Si-Fe_2O_3 in the voltage range of 0.01–2.8 V at a scan rate of 0.1 mV s^{-1}. During the first discharge process, two reduction peaks at 1.48 and 0.68 V can be observed, which could be related to a multi-step electrochemical reduction process.[6,52,53] Specifically, the small cathodic peak at 1.48 V can be ascribed to the initial lithium intercalation and the phase transition from hexagonal $Li_x(Fe_2O_3)$ to cubic $Li_2(Fe_2O_3)$.[54,55] In addition, another cathodic peak located around 0.68 V, which disappears from the second cycle, can be attributed to the further reduction of the $Li_2(Fe_2O_3)$ to Fe^0, as well as the formation of the solid electrolyte interphase (SEI) layer.[56] Thus, the reactions are speculated to be as follows:

$$Fe_2O_3 + 2Li^+ + 2e^- \rightarrow Li_2(Fe_2O_3) \quad (1)$$

$$Li_2(Fe_2O_3) + 4Li^+ + 4e^- \rightarrow 2Fe^0 + 3Li_2O \quad (2)$$

In addition, another cathodic peak at 0.18 V appears from the second cycle, which is attributed to the alloying of lithium with silicon.[57] The subsequent broad anodic peaks during the charge process are observed at 1.60 and 1.93 V, indicating the multiple step oxidation of Fe^0.[26,54,58] Meanwhile, the other oxidative peaks located at about 0.31 and 0.48 V are due to the extraction of lithium ions from the carbon and the de-alloying of Li_xSi.[7,35] The general overlapping of charge curves implies good reversibility and stability of the electrochemical reactions.[6] These results nearly coincide with the voltage plateaus in the galvanostatic discharge–charge curves [Fig. 5(a)] and are consistent with the good cycling performance of C-Si-Fe_2O_3, as discussed below. Compared with C-Si-Fe_2O_3, however, the first three CV curves of C-Si in Fig. S4 are quite different. Only the reduction peaks below 0.3 V and anodic peaks around 0.5 V can be found.

The cycling performance in Fig. 5(c) shows the charge/discharge capacity of C-Si-Fe_2O_3 at a current density of 750 mA g^{-1} for 220 cycles. It can be seen that the charge capacity is 1911.4 mAh g^{-1} at the first cycle and 1980.5 mAh g^{-1} after 220 cycles, suggesting that C-Si-Fe_2O_3 has high capacity and good cycling stability. Meanwhile, a small decrease in the reversible capacity is observed during the first 50 cycles. After that, the capacity starts to increase slowly and reaches a plateau after the 100th cycle. This kind of electrochemical performance is well coincide with the previous reported Si- or iron oxide-based anodes.[59-61] We believer, this phenomenon might be indicative of a change in the lithium ion insertion and extraction reactions after deep cycles, leading to the continuously various degree activation of the active materials. The exact reason for this performance is unclear at this stage, and further in-depth investigation is needed. It is well known that the capacity of AC is around 600.0 mAh g^{-1}.[62] Thus, the improved capacity for C-Si-Fe_2O_3 is attributed to the contribution of silicon and α-Fe_2O_3 nanoparticles, and the capacity of silicon, α-Fe_2O_3, and AC is calculated to be around 2730.0, 200.0, and 90.0 mAh g^{-1}, respectively (based on the CHN data). Therefore, the theoretical capacity of C-Si-Fe_2O_3 is around 3020.0 mAh g^{-1}, and the capacity retention is about 65.6 %, even after 220 cycles.

Fig. 5(d) shows the rate performance of the samples at different current densities. The charge capacities of C-Si-Fe_2O_3 and C-Si for the initial 0.75 A g-1 after 20 cycles are 1472.0 and 1148.3 mAh g^{-1}, respectively, and the retention of the capacity at 1.5, 3.0, and 6.0 A g^{-1} is 96.2, 66.0, and 50.4 % for C-Si-Fe_2O_3, respectively, higher than

the corresponding values for C-Si (61.2, 12.8, and 5.8%), especially at the current densities of 3.0 and 6.0 A g^{-1}, indicating the better rate performance of C-Si-Fe_2O_3. More importantly, compared with C-Si, after the high rate charge and discharge, a much higher reversible capacity of C-Si-Fe_2O_3 can still be maintained for the next 150 cycles. Fig. S5 shows the electrochemical impedance plots of C-Si-Fe_2O_3 and C-Si. It can be seen that the conductivity of C-Si-Fe_2O_3 is less than that of C-Si.[7]

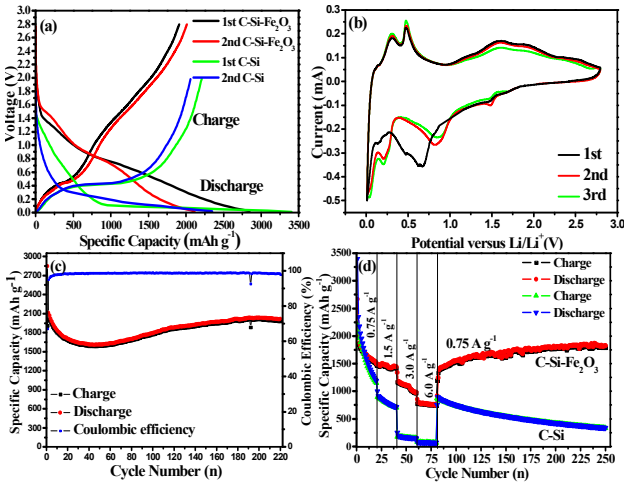

Fig. 5. Electrochemical properties: (a) the initial discharge-charge profiles of C-Si-Fe_2O_3 and C-Si, (b) the first three consecutive CV curves of C-Si-Fe_2O_3 at a scan rate of 0.1 mV s^{-1}, (c) the cycling performance of C-Si-Fe_2O_3 between 2.8 and 0.01 V at the current density of 750 mA g^{-1}, and (d) the rate performance of C-Si-Fe_2O_3 and C-Si at different current densities

The enhanced electrochemical properties of the porous C-Si-Fe_2O_3 could be attributed to its unique architecture: (1) the sandwiched nanoarchitecture helps to protect the α-Fe_2O_3 and Si NPs from agglomeration and enables good dispersion of these active particles over the carbon sheet supports; (2) the multilayered structure can provide a porous, highly conducting 3D network that can serve as a structural scaffold to improve the electronic conductivity, strengthen the mechanical properties, and also provide better room for the huge volume changes of Si NPs and α-Fe_2O_3 during cycling;[5,63,64] and (3) the nanosized α-Fe_2O_3 particles (～30 nm) uniformly embedded on the carbon layers will enhance the diffusion process, which leads to less tortuosity of the electrode and higher electrolyte diffusion, thus enhancing the rate performance.[65]

Conclusions

In summary, we have demonstrated a facile and scalable method for preparing a novel nanoarchitecture for carbon@silicon@hematite (C-Si-Fe_2O_3) composite, employing a one-step self-assembly method. Silicon nanoparticles are sandwiched between the nanosized iron-oxide-embedded carbon layers. The rationally designed unique 3D porous carbon network enhances the electrical conductivity and enables this C-Si-Fe_2O_3 composite to buffer the volume changes of silicon and α-Fe_2O_3 during the cycling much more effectively. Compared with commercial graphite microspheres (372 mAh g^{-1}), C-Si-Fe_2O_3 shows much higher capacity and better rate performance. Clearly, the simplicity and scalability of this fabrication process and its excellent electrochemical properties will make C-Si-Fe_2O_3 anode material promising for practical application in the next generation of Li-ion cells.

Acknowledgements

This work is supported by a BAJC (Baosteel-Australia Joint Research & Development Centre) project BA14006, an Auto CRC 2020, Project 1-117 and the National High-tech R&D Program of China (863 Program, No. 2015AA034601). Lei Zhang would like to thank CSC scholarships from China. The authors would like to also thank Dr. Tania Silver for critical reading of the manuscript and Dr. Dongqi Shi for XPS testing and also acknowledge the use of the facilities in the UOW Electron Microscopy Center, with particular thanks to Dr. Gilberto Casillas-Garcia.

References

1 J. B. Goodenough and Y. Kim, Chem. Mater., 2010, **22**, 587-603.
2 B. Dunn, H. Kamath and J. M. Tarascon, Science, 2011, **334**, 928-35.
3 M. Armand and J.-M. Tarascon, Nature, 2008, **451**, 652-657.
4 M. S. Whittingham, Chem. Rev, 2004, **104**, 4271-4301.
5 N. Liu, H. Wu, M. T. McDowell, Y. Yao, C. Wang and Y. Cui, Nano Lett., 2012, **12**, 3315-3321.
6 L. Li, H. B. Wu, L. Yu, S. Madhavi and X. W. D. Lou, Adv. Mater. Interface, 2014, **1**, 1400050.
7 L. Zhang, Y. Wang, G. Kan, Z. Zhang, C. Wang, Z. Zhong and F. Su, RSC Adv., 2014, **4**, 43114-43120.
8 N. Liu, Z. Lu, J. Zhao, M. T. McDowell, H. W. Lee, W. Zhao and Y. Cui, Nat. Nanotechnol., 2014, **9**, 187-92.
9 Y. Z. Xianjun Zhu, Shanthi Murali, Meryl D. Stoller, and Rodney S. Ruoff,, ACS Nano, 2011, **5**, 3333-3338.
10 A. M. Chockla, J. T. Harris, V. A. Akhavan, T. D. Bogart, V. C. Holmberg, C. Steinhagen, C. B. Mullins, K. J. Stevenson and B. A. Korgel, J. Am. Chem. Soc., 2011, **133**, 20914-20921.
11 X. Zhou, Y.-X. Yin, A.-M. Cao, L.-J. Wan and Y.-G. Guo, ACS Appl. Mater. Interfaces, 2012, **4**, 2824-2828.
12 H. Jia, P. Gao, J. Yang, J. Wang, Y. Nuli and Z. Yang, Adv. Energy Mater., 2011, **1**, 1036-1039.
13 B. Liu, X. Wang, H. Chen, Z. Wang, D. Chen, Y. B. Cheng, C. Zhou and G. Shen, Sci. Rep., 2013, **3**, 1622.
14 B. Z. Igor Kovalenko, Alexandre Magasinski, Benjamin Hertzberg, Zoran Milicev, Ruslan Burtovyy, Igor Luzinov, Gleb Yushin, Science, 2011, **334**, 75-79.
15 P. Y. C. Wu, X. Zhu, C. Yang, and Y. Xie, J. Phys. Chem. B, 2006, **110**, 17806-17812.
16 J. Yu, H. H. Zhan, Y. H. Wang, Z. L. I. Zhang, H. Chen, H. Li, Z. Y. Zhong and F. B. Su, J. Power Sources, 2013, **228**, 112-119.
17 P. Gu, R. Cai, Y. Zhou and Z. Shao, Electrochim. Acta, 2010, **55**, 3876-3883.
18 W. Wang and P. N. Kumta, ACS Nano, 2010, **4**, 2233-2241.
19 X. H. Liu, L. Zhong, S. Huang, S. X. Mao, T. Zhu and J. Y. Huang, ACS Nano, 2012, **6**, 1522-1531.
20 A. Kohandehghan, P. Kalisvaart, K. Cui, M. Kupsta, E. Memarzadeh and D. Mitlin, J. Mater. Chem. A, 2013, **1**, 12850-12861.

21 M. Ge, J. Rong, X. Fang and C. Zhou, Nano Lett., 2012, **12**, 2318-2323.
22 T. Song, J. Xia, J. H. Lee, D. H. Lee, M. S. Kwon, J. M. Choi, J. Wu, S. K. Doo, H. Chang, W. I. Park, D. S. Zang, H. Kim, Y. Huang, K. C. Hwang, J. A. Rogers and U. Paik, Nano Lett., 2010, **10**, 1710-1716.
23 M. Y. Ge, J. P. Rong, X. Fang, A. Y. Zhang, Y. H. Lu and C. W. Zhou, Nano Res., 2013, **6**, 174-181.
24 J. H. Kong, W. A. Yee, Y. F. Wei, L. P. Yang, J. M. Ang, S. L. Phua, S. Y. Wong, R. Zhou, Y. L. Dong, X. Li and X. H. Lu, Nanoscale, 2013, **5**, 2967-2973.
25 R. C. de Guzman, J. H. Yang, M. Ming-Cheng, S. O. Salley and K. Y. S. Ng, Asian J. Mater. Sci., 2013, **48**, 4823-4833.
26 L. X. Jun Chen, Weiyang Li, and Xinglong Gou, Adv. Mater., 2005, **17**, 582-586.
27 H. W. Nian Liu, Matthew T. McDowell, Yan Yao, Chongmin Wang, and Yi Cui, Nano Lett., 2012, **12**, 3315-3321.
28 Z.-J. Zhang, Y.-X. Wang, S.-L. Chou, H.-J. Li, H.-K. Liu and J.-Z. Wang, J. Power Sources, 2015, **280**, 107-113.
29 Y. Hwa, W. S. Kim, B. C. Yu, S. H. Hong and H. J. Sohn, J. Phys. Chem. C, 2013, **117**, 7013-7017.
30 W. N. Ren, C. Wang, L. F. Lu, D. D. Li, C. W. Cheng and J. P. Liu, J. Mater. Chem. A, 2013, **1**, 13433-13438.
31 Z. Xu, B. Zhang, S. Abouati, M. Garakani, J. Huang, J. Huang, E. Heidari and J. Kim, J. Mater. Chem. A, 2014, **2**, 17944-17951.
32 T. Song, H. Y. Cheng, H. Choi, J. H. Lee, H. Han, D. H. Lee, D. S. Yoo, M. S. Kwon, J. M. Choi, S. G. Doo, H. Chang, J. L. Xiao, Y. G. Huang, W. I. Park, Y. C. Chung, H. Kim, J. A. Rogers and U. Paik, Acs Nano, 2012, **6**, 303-309.
33 G. Grinbom, D. Duveau, G. Gershinsky, L. Monconduit and D. Zitoun, Chem. Mater., 2015, **27**, 2703-2710
34 J. K. Lee, K. B. Smith, C. M. Hayner and H. H. Kung, Chem. Commun., 2010, **46**, 2025-7.
35 X. L. Bin Wang, Xianfeng Zhang, Bin Luo, Meihua Jin, Minghui Liang, Shadi A. Dayeh, S. T. Picraux, and Linjie Zhi, ACS Nano, 2013, **7**, 1437-1445.
36 J. Z. Xianghong Liu, Wenping Si, Lixia Xi, Barbara Eichler, Chenglin Yan, and Oliver G. Schmidt, ACS Nano, 2015, **9**, 1198-1205.
37 J. Chang, X. Huang, G. Zhou, S. Cui, P. B. Hallac, J. Jiang, P. T. Hurley and J. Chen, Adv Mater, 2014, **26**, 758-64.
38 L. Chen, Z. Wang, C. He, N. Zhao, C. Shi, E.-Z. Liu and J. Li, ACS Appl. Mater. Interfaces, 2013, **5**, 9537-9545.
39 B. Jang, M. Park, O. B. Chae, S. Park, Y. Kim, S. M. Oh, Y. Piao and T. Hyeon, J. Am. Chem. Soc., 2012, **134**, 15010-5.
40 J. Park, K. An, Y. Hwang, J. G. Park, H. J. Noh, J. Y. Kim, J. H. Park, N. M. Hwang and T. Hyeon, Nat. Mater., 2004, **3**, 891-895.
41 X. Zhu, H. Chen, Y. Wang, L. Xia, Q. Tan, H. Li, Z. Zhong, F. Su and X. Zhao, J. Mater. Chem. A, 2013, **1**, 4483-4489.
42 J. I. Lee, K. T. Lee, J. Cho, J. Kim, N. S. Choi and S. Park, Angew. Chem., 2012, **124**, 2821-2825.
43 S. Ray, C. Pao, H. Tsai, B. Bose, J. Chiou, W. Pong and D. DasGupta, Carbon, 2006, **44**, 1982-1985.
44 L. Ji and X. Zhang, Carbon, 2009, **47**, 3219-3226.
45 F. Su, X. Zhao, Y. Wang, J. Zeng, Z. Zhou and J. Y. Lee, J. Phys. Chem. B, 2005, **109**, 20200-20206.
46 A. Cuesta, P. Dhamelincourt, J. Laureyns, A. Martinez-Alonso and J. M. Tascón, J. Mater. Chem., 1998, **8**, 2875-2879.
47 Q. Yang, W. Xu, A. Tomita and T. Kyotani, J. Am. Chem. Soc., 2005, **127**, 8956-8957.
48 J. Zhang, X. Liu, L. Wang, T. Yang, X. Guo, S. Wu, S. Wang and S. Zhang, Nanotechnology, 2011, **22**, 185501.
49 Y. G. Guo, J. S. Hu and L. J. Wan, Adv. Mater., 2008, **20**, 2878-2887.
50 A. Mabuchi, K. Tokumitsu, H. Fujimoto and T. Kasuh, J. Electrochem. Soc., 1995, **142**, 1041-1046.
51 Y. Liu, J. Xue, T. Zheng and J. Dahn, Carbon, 1996, **34**, 193-200.
52 C. T. Cherian, J. Sundaramurthy, M. Kalaivani, P. Ragupathy, P. S. Kumar, V. Thavasi, M. V. Reddy, C. H. Sow, S. G. Mhaisalkar, S. Ramakrishna and B. V. R. Chowdari, J. Mater. Chem., 2012, **22**, 12198-12204.
53 D. Larcher, D. Bonnin, R. Cortes, I. Rivals, L. Personnaz and J. M. Tarascon, J. Electrochem. Soc., 2003, **150**, A1643-A1650.
54 J. Luo, X. Xia, Y. Luo, C. Guan, J. Liu, X. Qi, C. F. Ng, T. Yu, H. Zhang and H. J. Fan, Adv. Energy Mater., 2013, **3**, 737-743.
55 S.-L. Chou, J.-Z. Wang, D. Wexler, K. Konstantinov, C. Zhong, H.-K. Liu and S.-X. Dou, J. Mater. Chem., 2010, **20**, 2092-2098.
56 Y. Luo, D. Kong, J. Luo, Y. Wang, D. Zhang, K. Qiu, C. Cheng, C. M. Li and T. Yu, RSC Adv., 2014, **4**, 13241-13249.
57 Y.-X. Wang, S.-L. Chou, J. H. Kim, H.-K. Liu and S.-X. Dou, Electrochim. Acta, 2013, **93**, 213-221.
58 D. Larcher, C. Masquelier, D. Bonnin, Y. Chabre, V. Masson, J. B. Leriche and J. M. Tarascon, J. Electrochem. Soc., 2003, **150**, A133-A139.
59 J. Luo, J. Liu, Z. Zeng, C. Ng, L. Ma, H. Zhang, J. Lin, Z. Shen, and H. Fan, Nano lett. 2013, **13**, 6136−6143.
60 L. Zhang, R. Rajagopalan, H. Guo, X. Hu, S. Dou, and H. Hua, Adv. Funct. Mater., 2015, DOI: 10.1002/adfm.201503777.
61 J. Chang, X. Huang, G. Zhou, S. Cui, P. Hallac, J. Jiang, P. Hurley, and J. Chen. Adv. Mater., 2014, **26**, 758-764.
62 L. Zhang, M. Zhang, Y. Wang, Z. Zhang, G. Kan, C. Wang, Z. Zhong and F. Su, J. Mater. Chem. A, 2014, **2**, 10161-10168.
63 A. Vu, Y. Qian and A. Stein, Adv. Energy Mater., 2012, **2**, 1056-1085.
64 T. Cetinkaya, M. Uysal, M. O. Guler, H. Akbulut and A. Alp, Powder Technol., 2014, **253**, 63-69.
65 M. Ebner, D.-W. Chung, R. E. García and V. Wood, Adv. Energy Mater., 2014, **4**, 1301278.